Environmental Science Advances

ROYAL SOCIETY OF CHEMISTRY

PAPER

View Article Online
View Journal | View Issue

Cite this: *Environ. Sci.: Adv.*, 2023, **2**, 98

Sequencing batch photocatalytic H_2O_2 production over a magnetic resorcinol–formaldehyde polymer for on-site water purification by UV light irradiation†

Jingzhen Zhang,[a] Qian Zheng,[a] Chen Chen,[b] Xiangcheng Zhang,[a] Xiaoyan Guo[c] and Mingce Long *[a]

Received 25th September 2022
Accepted 27th October 2022

DOI: 10.1039/d2va00228k

rsc.li/esadvances

A self-maintainable decentralized water treatment system is appealing, while avoiding chemical addition is the prerequisite to realize it. As a widely used chemical in advanced oxidation processes (AOPs), H_2O_2 can be produced *via* photocatalysis. However, there remain challenges to use the photocatalytically produced H_2O_2 for water purification in a continuous operation, which requires that the produced H_2O_2 solution has no impurity and the catalyst powder is easily separable. We realized this by photocatalytic H_2O_2 production over magnetic separable photocatalytic microspheres through a sequencing batch process and coupling with ultraviolet C (UVC)/H_2O_2 for micropollutant removal *via* a flow-through operation. The photocatalysts were synthesized by *in situ* growth of a resorcinol–formaldehyde (RF) copolymer on Fe_3O_4@SiO_2 microspheres, which can convert earth-abundant water and air into H_2O_2 under visible light irradiation. A clean H_2O_2 solution was produced at 100 μmol h^{-1} g^{-1} over magnetic photocatalysts and separated by using an external magnetic field. The on-site utilization of the obtained H_2O_2 solution was realized *via* UV light irradiation. This work provides a rational design of easily separable photocatalysts for H_2O_2 production, and offers insights for development of water purification processes with zero chemical addition and maintenance.

Environmental significance

Maintenance and chemicals account for a large part of the cost in diverse technologies for water purification. Thus, a self-maintainable decentralized water treatment system with zero commercial chemicals is appealing for sustainable water cleanup, especially significant for rural areas. Solar-driven H_2O_2 production and *in situ* activation provide the possibility to develop an advanced oxidation process with zero chemicals and maintenance. We coupled photocatalytic H_2O_2 production and UVC activation in a flow-through operation for organic micropollutant removal in water. This process was realized by developing magnetic separable resorcinol–formaldehyde photocatalysts on Fe_3O_4@SiO_2 microspheres, which can produce H_2O_2 solution by facile cycling of catalysts. This work provides a promising way to develop water purification processes with zero chemical addition and maintenance.

Introduction

Hydrogen peroxide (H_2O_2)-based advanced oxidation processes (AOPs) have been widely applied to remove persistent organic micropollutants in water by producing strong oxidative species like hydroxyl radicals (˙OH).[1–3] Among these AOPs, ultraviolet (UV)/H_2O_2 is the most effective one to remove diverse organic pollutants just by using electrical energy (for UV light) and H_2O_2 to produce ˙OH at a high quantum yield (up to 100%).[4–6] The cost of this process is the sum of electrical energy and oxidant costs, in which maintenance accounts for up to 45% of the electrical energy cost.[7,8] A great number of efforts have been made to enhance the removal efficiency and decrease the operation cost by using additional chemicals (*e.g.* persulfate) and optimizing reactors.[9–11] However, it would be effective to minimize the cost by developing a process that avoids chemical addition and maintenance. This is especially significant for decentralized water purification in rural areas.

The current commercial production of H_2O_2 is based on an anthraquinone process, which is limited by the costly hydrogen gas, noble metal catalysts, toxic organic solvents, and high-energy inputs.[12,13] Moreover, the storage and transportation of

[a]*School of Environmental Science and Engineering, Key Laboratory of Thin Film and Microfabrication Technology, Ministry of Education, Shanghai Jiao Tong University, Shanghai 200240, China. E-mail: long_mc@sjtu.edu.cn*

[b]*Shanghai Waterway Engineering Design and Consulting Co., Ltd, Shanghai 200120, China*

[c]*Key Laboratory of Pollution Processes and Environmental Criteria, College of Environmental Science and Engineering, Ministry of Education, Nankai University, Tianjin 300350, China*

† Electronic supplementary information (ESI) available. See DOI: https://doi.org/10.1039/d2va00228k

the concentrated H_2O_2 (above 30%) is hazardous, and dilution is necessary in the further utilization for water purification.[4,14] This makes the maintenance of the H_2O_2-involved processes inevitable. Photocatalytic H_2O_2 production by converting earth-abundant H_2O and O_2 over photocatalysts is an emerging approach to produce H_2O_2 at mild concentrations on a small scale.[15–17] In this solar-to-chemical process, the two-electron oxygen reduction reaction (ORR) for H_2O_2 synthesis is enabled by photogenerated electrons, while water is oxidized by photogenerated holes and synchronously offers protons.[18–20] Photocatalytic H_2O_2 production displays great potential for diverse water purification applications,[21,22] while the development of efficient photocatalysts is the prerequisite to realize it. Among the photocatalysts for H_2O_2 production, the resorcinol–formaldehyde (RF) copolymer, a metal-free photocatalyst, possesses a narrow bandgap (2.0 eV) and a wide absorption region (up to 700 nm). Under sunlight irradiation, H_2O_2 can be produced over an RF copolymer in pure water with a relatively high solar-to-H_2O_2 conversion efficiency (0.5%).[23,24] However, this RF material exhibits a form of powder with low density and poor dispersion, resulting in challengeable separation. Immobilizing the photocatalysts on porous substrates is one feasible choice but significantly decreases mass transfer and H_2O_2 production. The downstream separation such as membrane filtration is energy-costing, and organic membranes are labile in H_2O_2 solution.[25,26] Thus, facile separation of photocatalyst powder to ensure production of a clean H_2O_2 solution is a prerequisite for the integration of H_2O_2 production and on-site utilization for water purification.

Magnetic nanomaterials such as Fe_3O_4 nanoparticles can be easily collected and recovered by using external magnetic fields, and the recovery of water can reach 100% after magnetic separation.[27–29] These materials are usually used as catalyst supports to improve recyclability.[8,30,31] Herein, we report a strategy to develop magnetic separable photocatalysts by *in situ* growing RF layers on silica-coated magnetite microspheres, and developed a process integrating photocatalytic H_2O_2 synthesis and on-site UVC activation to remove organic pollutants in water. This process displays great potential to be operated without any chemical addition and maintenance.

Experimental section

Synthesis of catalysts

Fe_3O_4 magnetic nanoparticles. Fe_3O_4 magnetic nanoparticles were synthesized by a solvothermal method.[32] 2.7 g of iron(III) chloride hexahydrate (98%, Sinopharm) and 7.2 g of sodium acetate (98%, Sinopharm) were dissolved in 100 mL of ethylene glycol (98%, Aladdin Biochemical Technology) and stirred for 10 min to form a clear yellow solution. Then, the homogeneous solution was transferred into a Teflon-lined stainless steel autoclave (100 mL) and heated at 200 °C for 8 hours. Then the autoclave was cooled down to room temperature, and the black product was washed with ethanol and water, separated and vacuum dried at 60 °C for 12 hours to obtain Fe_3O_4 magnetic nanoparticles.

Fe_3O_4@SiO_2 microspheres. The Stöber method was employed to form a SiO_2 layer over the Fe_3O_4 surface. The as-prepared Fe_3O_4 nanoparticles (0.10 g) were pre-treated in 50 mL hydrochloric acid solution (0.1 M) under 10 min ultrasonication. After washing and separation, the pre-treated Fe_3O_4, 1.5 mL ammonia solution (28 wt%, Sinopharm) and 1.86 g tetraethyl orthosilicate (TEOS, 98%, Aladdin Biochemical Technology) were added into 100 mL of 80 vol% ethanol solution, followed by stirring at room temperature for 360 min. Finally, Fe_3O_4@SiO_2 microspheres were obtained after washing, filtering and drying under vacuum at 60 °C for 6 hours.

Magnetic resorcinol–formaldehyde photocatalysts. Fe_3O_4@SiO_2 microspheres (0.1 g), ammonia (0.1 mL, 28 wt% Sinopharm) and cetyltrimethylammonium bromide (CTAB, 0.01 mmol, 99%, Sigma-Aldrich) were mixed in 30 mL of deionized water and stirred for 30 min. Then, 4.5 mmol of resorcinol (99%, Sigma-Aldrich) and 8.2 mmol of formaldehyde solution (33 wt%, Sinopharm) were added into the mixture and mechanically stirred for 16 hours. Then, the suspension was transferred into a Teflon-lined stainless steel autoclave (50 mL) and kept at 210 °C for 24 hours. The obtained black samples are magnetic resorcinol–formaldehyde catalysts, which were labeled as MRF. MRF-0.5 and MRF-2.0 were synthesized according to the same procedure as MRF, but the dosages of resorcinol and formaldehyde were half and double of those used in MRF synthesis, respectively. RF photocatalysts were prepared *via* the same procedure but without magnetic particles.

Characterization

The morphology of materials was recorded by using a Talos F200X scanning transmission electron microscope (TEM, FEI, USA). The accelerating voltage for each test is 200 kV. The X-ray diffraction (XRD) patterns of samples were collected on a Rigaku D/max-2200 PC X-ray diffractometer with Cu-Kα radiation ($\lambda = 0.154$ nm, 40.0 kV and 30.0 mA). The Fourier transform infrared (FTIR) spectra were recorded on a Thermo Electron Nicolet 6700 spectrometer. X-ray photoelectron spectra (XPS) were recorded on a Shimadzu-Kratos spectrometer (Al Kα radiation, 2×10^{-9} Pa) with an Axis Ultra DLD system. The BET specific surface area and pore volume analyses were carried out on a gas sorption analyzer (Quantachrome Autosorb-IQ3). Thermogravimetric analysis (TGA) and differential scanning calorimetry (DSC) were carried out on a Mettler-Toledo analyzer (TGA/DSC1/1600HT). The temperature is increased from 20 to 800 °C (10 °C min^{-1}) in an air atmosphere (30 mL min^{-1}). Magnetic properties of the materials were measured on a SQUID-based vibrating sample magnetometer (VSM, MPMS-3, Quantum Design) at room temperature.

Photocatalytic reaction

Photocatalytic H_2O_2 production was conducted in a 50 mL quartz cuvette. Typically, 30 mg of catalysts were dispersed in 30 mL of pure water. During the tests, a Xe lamp (PLS-SXE300, 300 W) with a cut-off filter ($\lambda > 420$ nm) provided visible-light irradiation, and the suspension was continuously purged with

air. The dissolved O_2 concentration was measured by using a fiber optic oxygen meter (OXY-1 SMA, PreSens Precision Sensing GmbH, Germany). The magnetic catalysts can be separated by using a magnet for the cycle tests. Photocatalytic H_2O_2 decomposition was carried out in a H_2O_2 suspension (1000 μM) containing 1 g L^{-1} of catalysts in a N_2 atmosphere under visible-light irradiation ($\lambda > 420$ nm). The H_2O_2 concentration was determined by the *N*,*N*-diethyl-*p*-phenylenediamine (DPD, 97%)-horseradish peroxidase (POD, RZ > 1.5) method.[33,34]

Organic pollutants including rhodamine B (RhB), humic acid (HA) and tetracycline (TC) were degraded *via* a UVC/H_2O_2 coupling with photocatalytic H_2O_2 production. In a typical test, H_2O_2 was generated by using a 150 mL MRF suspension (1 g L^{-1}) after 60 min visible light irradiation with air purging. Then, the catalysts were separated from water by using a magnetic field, and the H_2O_2 solution was used for wastewater treatment. Both batch and flow-through tests were carried out to evaluate organic degradation in the UVC/H_2O_2 processes. In a batch operation, 5 mL of H_2O_2 aqueous solution (100 μM) was mixed with 45 mL wastewater and irradiated under a UVC light for 60 min. The UVC light source was six G4T5 bulbs (Sankyo Denki, $\lambda = 254$ nm, 4 W). In a flow-through operation, 200 mL of H_2O_2 solution (100 μM) was mixed with 1800 mL of wastewater containing a certain concentration of organic micropollutants (RhB, HA or TC). Then, the mixture was pumped into a UVC reactor at 10, 20 or 30 mL min^{-1} flow rate. The section view of UVC reactor is shown in Fig. S1.† A UVC lamp (Cnlight, $\lambda = 254$ nm, 15 W) was used and the effective volume for wastewater treatment was 1000 mL. The concentration of RhB, HA and TC was measured by using a UV-vis spectrophotometer (TU-1810, Beijing Purkinje) at 564, 254 and 357 nm, respectively. The electrical energy per order (E_{EO}) in the flow-through operation is calculated using eqn (1):[35]

$$E_{EO} = \frac{P}{F \lg(C_i/C_f)} \quad (1)$$

where, P is the power of the UVC light (kW); F is the volume flow rate of water (m^3 h^{-1}); C_i and C_f are the initial and final concentrations of micropollutants (mg L^{-1}), respectively.

Results and discussion

Characterization of MRF microspheres

The magnetic resorcinol–formaldehyde (MRF) photocatalyst was synthesized by the procedure described in Fig. 1A. Fe_3O_4 nanoparticles have superparamagnetism and have been frequently used as the magnetic core for magnetic separable core–shell materials. To prevent the aggregation and possible etching of Fe_3O_4 nanoparticles by reacting with H_2O_2,[36] a layer of SiO_2 coating is incorporated on the surface of Fe_3O_4 due to its good compatibility and hydrophilicity.[37,38] However, under the alkaline conditions for the polycondensation of RF (pH > 10), the SiO_2 layer would be negatively charged. Considering that the surface of RF particles is also negative,[37] and electrostatic repulsive force between the two components would accordingly inhibit the formation of RF over SiO_2, a cationic surfactant (CTAB) is employed to render the surface of silica layers

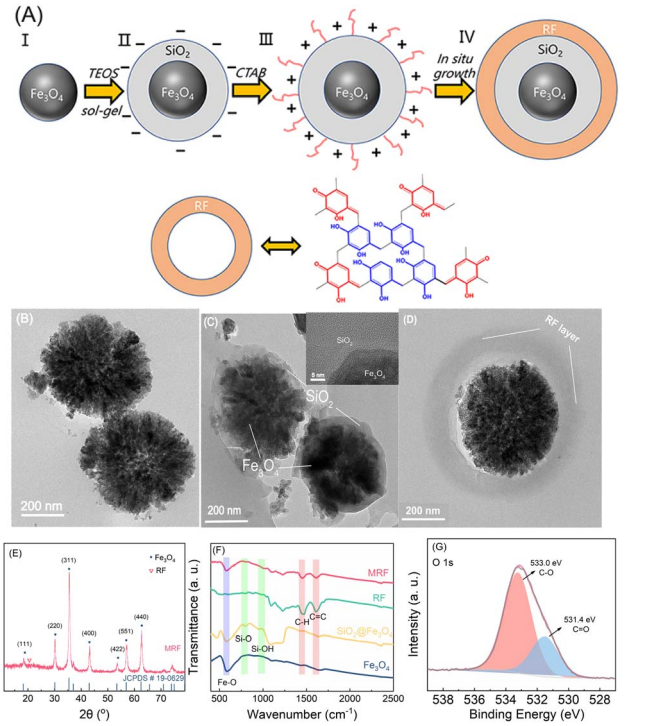

Fig. 1 (A) Schematic synthetic procedure of the magnetic resorcinol–formaldehyde photocatalysts; (B)–(D) TEM images of (B) Fe_3O_4 particles, (C) Fe_3O_4@SiO_2 (inset: HRTEM image at the core–shell interface), and (D) MRF microspheres; (E) XRD patterns of MRF; (F) FTIR spectra of various materials; (G) high-resolution O 1s XPS spectrum of MRF.

positively charged. Thus, the RF shell layer eventually *in situ* formed over silica-coated Fe_3O_4 microspheres.

As shown in Fig. 1B, Fe_3O_4 nanoparticles are prepared *via* a solvothermal method, and the as-synthesized spherical particles possess a mean diameter of 500 nm. Then, a silica layer about 50 nm of thickness is coated over the surface of Fe_3O_4 microspheres (Fig. 1C). No lattice fringe is observed in the SiO_2 region (inset in Fig. 1C), indicating that the SiO_2 layer is dominated by the amorphous phase.[39,40] CTAB induces a positively charged surface of Fe_3O_4@SiO_2, and then the RF copolymer as the shell layer is formed over Fe_3O_4@SiO_2 *via* a Stöber-like method.[22,39] The thickness of this shell layer is about 100 nm (Fig. 1D).

The crystalline structure of the catalyst is determined using powder XRD patterns (Fig. 1E). The diffraction pattern of MRF matches well with the JCPDS card 19-0629 for the face-centered cubic Fe_3O_4 phase.[41,42] The diffraction peaks at 30.2°, 35.6°, 43.3°, 57.2° and 62.8° correspond to the (220), (311), (400), (551) and (440) planes of cubic Fe_3O_4, respectively. A broad diffraction band at about 20° can be attributed to the (002) planes of graphitic carbon, suggesting the presence of π-stacking benzenoid–quinoid couples.[22,43] The surface functional groups of MRF were also analyzed using FTIR spectra (Fig. 1F). The peak at 586 cm^{-1} corresponds to the stretching metal–oxygen vibration of the Fe–O groups.[44,45] The weak bands at 798 and 956 cm^{-1} are assigned to the Si–O and Si–OH groups, respectively.[46] The bands located at 1615 and 1450 cm^{-1} correspond to the

stretching vibration of the aromatic C=C and C–H groups of the methylene linker, respectively.[47,48] The benzenoid–quinoid D–A resorcinol couples of the RF copolymer layers in MRF were proved by XPS spectra. The deconvoluted peaks in the C 1s (at 286.2 eV and 288.0 eV) (Fig. S2†) and O 1s (at 533.0 eV and 531.4 eV) XPS spectra (Fig. 1G) are assigned to the C–O and C=O bonds, corresponding to the benzenoid and quinoid forms in the RF framework, respectively.[21] The ratio of C–O/C=O obtained according to the data of the O 1s spectrum is 2.5. Thus, a shell of the RF copolymer was successfully formed over the Fe_3O_4@SiO_2 cores.

Photocatalytic H_2O_2 production over MRF microspheres

Fig. 2A reveals the time-dependent H_2O_2 production in water over different materials under visible light. Fe_3O_4@SiO_2 microspheres and Fe_3O_4 nanoparticles produce negligible H_2O_2, indicating that the support materials for RF have no photocatalytic activity. Using MRF (1 g L^{-1}) as the photocatalyst, H_2O_2 concentrations increase linearly with time, achieving a H_2O_2 production rate of 100 μM h^{-1} under air purging conditions, in which the dissolved oxygen concentration is about 10 mg L^{-1}. When the suspension is purged with O_2, the dissolved O_2 increases to about 40 mg L^{-1}, and the photocatalytic H_2O_2 production within 60 min is enhanced to 150 μM. However, when purging with N_2, the system produces negligible H_2O_2, suggesting that the oxygen reduction is the main pathway for H_2O_2 production.[49–51] Upon 12 hours of irradiation under air purging conditions, MRF can produce 1200 μM H_2O_2 without any retardation (Fig. S3†), which is a relatively high value in the systems of photocatalytic H_2O_2 production in the absence of any organic sacrificial agent (Table S1†).

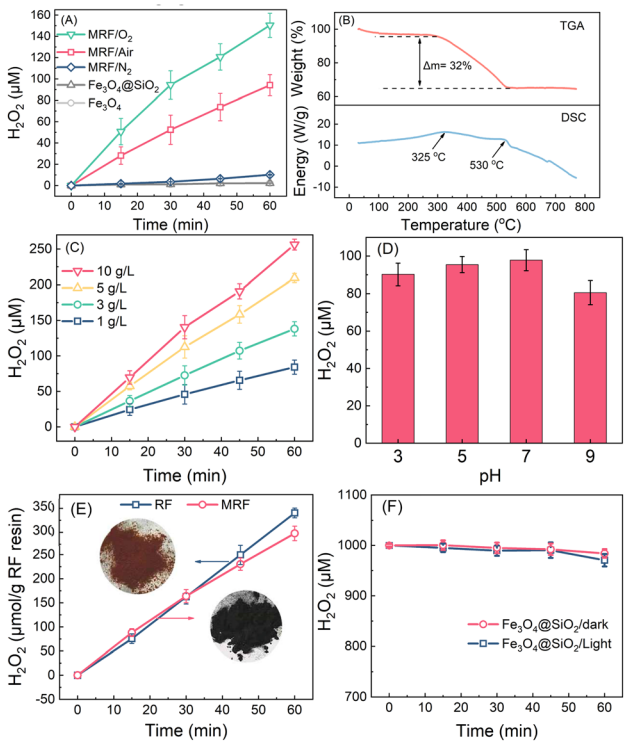

Fig. 2 (A) Photocatalytic H_2O_2 production over different materials (catalysts: 1 g L^{-1}; pH = 7.5; λ > 420 nm; O_2/air/N_2: 0.5 L min^{-1}); (B) TGA and DSC profiles for MRF pyrolysis; photocatalytic H_2O_2 production within 60 min (C) over different dosages of MRF and (D) over 1 g L^{-1} MRF at different pH values; (E) normalized H_2O_2 production over per gram of RF copolymers under air purging conditions; and (F) H_2O_2 decomposition over Fe_3O_4@SiO_2 in the dark and under visible-light irradiation (catalysts: 1 g L^{-1}; $[H_2O_2]_0$: 1000 μM; pH = 7.5; λ > 420 nm; N_2: 0.5 L min^{-1}).

The ratios of RF to Fe_3O_4@SiO_2 in MRF are optimized by measuring the performance of photocatalytic H_2O_2 production. The dosage of resorcinol and formaldehyde for MRF-0.5 and MRF-2.0 are 0.5-fold and 2.0-fold of that for MRF, respectively. As shown in Fig. S4,† H_2O_2 production over MRF-0.5 is 0.8-fold of that of MRF, while this over MRF-2.0 is only a 10% increase by comparing with that produced by MRF, suggesting that the content of RF polymers in MRF is nearly enough for photocatalytic H_2O_2 production. Thus, MRF is used for further tests due to its ratio of RF to Fe_3O_4@SiO_2 being optimal.

The weight percentage of the RF polymer in MRF was measured by the TGA-DSC analysis under air purging conditions (Fig. 2B). A two-stage weight loss can be observed in the TGA curve. Below 300 °C, weight loss is less than 3%, which can be ascribed to the removal of moisture in the materials. In the range of 300–550 °C, the weight loss is about 32%, accompanied by two exothermic peaks at 325 and 530 °C. This is associated with the decomposition of the RF polymer. When the temperature increases to above 550 °C, the weight percentage of MRF remains at 65%, corresponding to the inorganic component in the material. Thus, considering 65% inorganic components and 3% moisture in the material, the weight percentage of the RF copolymer in MRF is about 32%. According to the N_2 adsorption/desorption isotherm and the pore-size distribution curves of MRF (Fig. S5†), the specific surface area and total pore volume of this catalyst are 16.0 m^2 g^{-1} and 5.3 × 10^{-2} cm^3 g^{-1}, respectively. This indicates that MRF is a nonporous material, and the photocatalytic ORR mainly takes place over the surface layer.

H_2O_2 production increases with the increase of MRF dosages in the suspension (Fig. 2C). In the presence of 5 g L^{-1} and 10 g L^{-1} of MRF, the produced H_2O_2 in 60 min reaches 200 and 250 μM, respectively. H_2O_2 production on MRF shows a minor decrease with the increase of pH from 3 to 9, while above 80 μM upon 60 min irradiation at all the pH values (Fig. 2D). These results suggest that MRF displays a high and stable activity over a wide pH range, and continuous photocatalytic H_2O_2 production in pure water can be achieved by using a high dosage of MRF.

Considering that the weight percentage of RF in MRF is about 32%, the H_2O_2 production rate is normalized according to the weight of the RF copolymer, and the results are shown in Fig. 2E. In a control test, the pristine RF copolymer produces 300 μM H_2O_2 in 60 min, which is 3-fold that on MRF under the same conditions (Fig. S6†). Thus, the normalized H_2O_2 production of MRF is close to the theoretical value based on the pristine RF copolymer (Fig. 2E), suggesting negligible H_2O_2 decomposition on the Fe_3O_4@SiO_2 component in MRF

microspheres. This is further proved by measuring H_2O_2 decomposition over Fe_3O_4@SiO_2 under both dark and illumination conditions. As shown in Fig. 2F, in the N_2-purging Fe_3O_4@SiO_2 suspension, H_2O_2 concentration declines less than 2%, indicating that the as-prepared magnetic support materials do not consume H_2O_2 and affect H_2O_2 production. This is attributed to the tight layers of RF and SiO_2 blocking the access of H_2O_2 to core materials.[28,38]

The magnetization properties of materials are proved by VSM analysis. As shown in the magnetic hysteresis loops (Fig. 3A), the saturation magnetization (Ms) values for Fe_3O_4, Fe_3O_4@SiO_2 and MRF are 80.5, 60.6 and 59.9 emu g^{-1}, respectively. Moreover, negligible remanence or coercivity of all the curves are detected, proving the super-paramagnetism of these materials. As a result, MRF particles that disperse well in water can be rapidly aggregated in the presence of an external magnetic field (inset in Fig. 3A), and the recovery of MRF is over 99%. The characters and photocatalytic activity of the reused MRF after 12 h of prolonged irradiation were measured. As shown in the XPS spectrum of recovered MRF after the photocatalytic reaction (Fig. S7†), the changes of the band for the C=O bond are negligible. The TEM (Fig. S8†) and FTIR spectra (Fig. 3B) are almost the same as those of the fresh materials, indicating that the changes of the functional groups and microstructures of MRF are negligible. After five-cycle experiments, the H_2O_2 yield and the saturation magnetization of MRF (1 g L^{-1}) remain at 100 μM h^{-1} and 59.6 emu g^{-1} (Fig. 3C and D). The recovered MRF maintains the activity for H_2O_2 production and the magnetization for rapid separation. The total organic carbon (TOC) of the solution after removing MRF was 0.5 mg L^{-1}, which is almost the same as that of the control of deionized water, suggesting that the organic components in the material scarcely dissolve. Thus, the MRF photocatalysts display superior stability and easy recyclability, which enables ready utilization of the produced H_2O_2 for *on situ* usage.

On situ H_2O_2 utilization for decontamination *via* UVC irradiation

A process combining H_2O_2 production and *on situ* utilization for organic micropollutant removal is proposed (Scheme 1). In one cycle of the test, MRF (150 mg) is firstly dispersed in water (150 mL) by purging with air (I). Then, upon visible light irradiation, free electrons and holes are generated for the two-electron ORR and four-electron WOR, respectively (II). In this step, about 100 μM of H_2O_2 is produced per hour. Subsequently, MRF particles rapidly aggregate under the magnetic field and get separated from the H_2O_2 solution. After withdrawing the magnetic field, the catalysts are re-dispersed in fresh water and are ready for the next cycle (III). After three cycles, about 400 mL of the H_2O_2 solution at 100 μM concentration (40 μmol of H_2O_2) can be collected. The major energy consumption in photocatalysis comes from a 300 W xenon lamp, which can be conveniently replaced by sunlight. The H_2O_2 solution generated from photocatalysis mixes with the micropollutant-containing wastewater, and is then treated by UVC light irradiation through a batch or a flow-through operation.

In the batch operation, 5 mL of H_2O_2 solution (100 μM) was added into 45 mL of wastewater, resulting in the initial H_2O_2 and pollutant (RhB, HA, or TC) concentrations of 10 μM and 1 mg L^{-1}, respectively. The wastewater containing H_2O_2 was irradiated by using UVC light for 60 min. As shown in Fig. 4A, under dark conditions, the reduction of RhB, HA, and TC in the presence of 10 μM H_2O_2 is negligible. In the absence of H_2O_2 but upon UVC irradiation alone for 60 min, HA and TC have

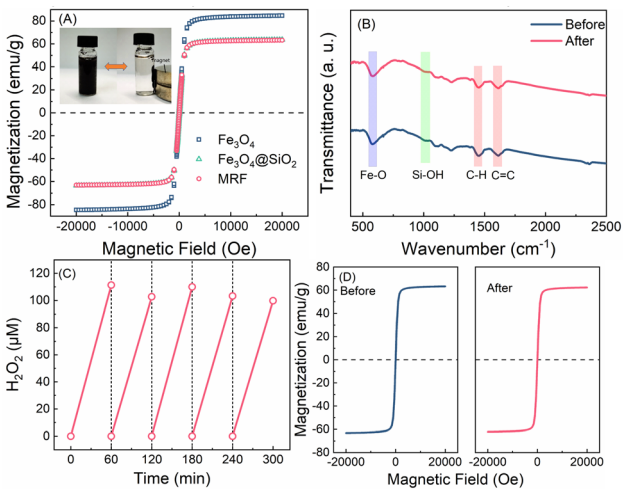

Fig. 3 (A) Magnetic hysteresis loops of the catalysts at room temperature and (A inset) magnetic separation and redispersion process of MRF; (B) FTIR spectra of MRF and reused MRF; repeated photocatalytic H_2O_2 production (C) and magnetic hysteresis loops (D) of reused MRF (catalysts: 1 g L^{-1}; pH = 7.5; λ > 420 nm; air: 0.5 L min^{-1}).

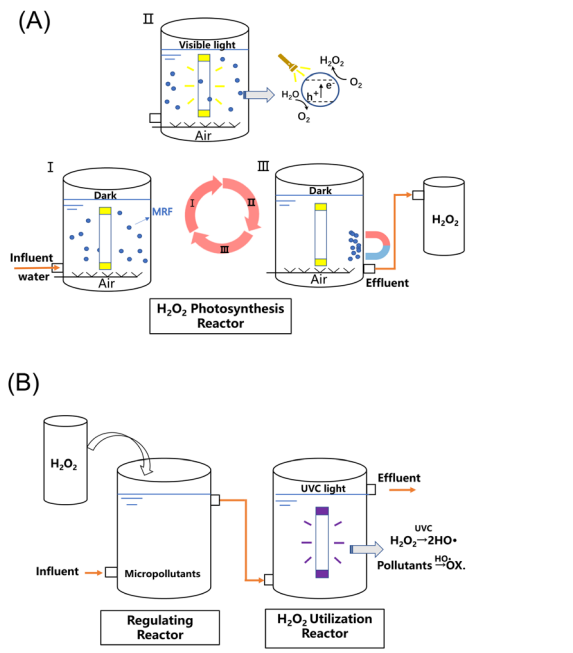

Scheme 1 Schematic illustration of sequencing batch photocatalytic H_2O_2 production over MRF (A) and UVC/H_2O_2 flow-through processes (B) for organic micropollutant degradation.

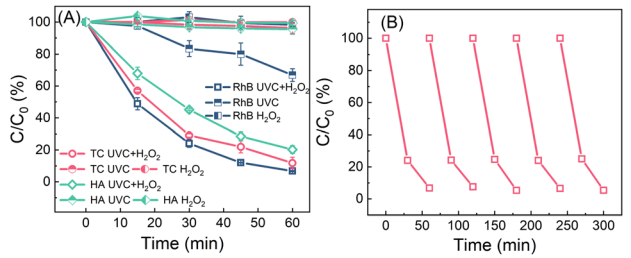

Fig. 4 (A) The removal of RhB, TC and HA *via* UVC/H_2O_2, UVC and H_2O_2 processes in batch tests; and (B) recyclability of the process for RhB removal (RhB, TC or HA: 1 mg L^{-1}; H_2O_2: 10 μM).

negligible reduction, while RhB has about 33.1% reduction. However, in the UVC/H_2O_2 system, the concentrations of RhB, HA and TC decrease to 0.05, 0.15 and 0.2 mg L^{-1} in 60 min, respectively. Owing to the UVC-induced H_2O_2 activation, hydroxyl radicals are produced to oxidize these organic pollutants.[52,53] The decay curve exhibits first-order reaction kinetics, and the rate constants for RhB, HA and TC are 0.045, 0.035 and 0.027 min^{-1}, which are about 6.7, 52.6 and 34.6-fold values of that treated by UVC irradiation in the absence of H_2O_2, respectively (Fig. S9†). The performance of RhB degradation *via* a sequencing batch process scarcely declines even after five cycles (Fig. 4B), indicating that this process exempted from external chemicals is robust to remove organic micropollutants in water.

In a flow-through operation, 1 mg L^{-1} of RhB (HA or TC) wastewater containing 10 μM of H_2O_2 produced from MRF photocatalysis were pumped into a UVC reactor at a 10 mL min^{-1} flow rate. The retention time for the wastewater is 100 min. As shown in Fig. 5, under UVC irradiation or H_2O_2-alone treatment, the RhB concentration in the effluent is about 0.20 and 0.99 mg L^{-1}. The significant removal of RhB by UVC irradiation alone in the flow-through operation can be attributed to the prolonged irradiation time. However, upon UVC irradiation, the RhB concentration in the H_2O_2-containing water decreases to below 0.01 mg L^{-1}, and the pink wastewater completely bleaches. The treatment also achieves high removal efficiencies for HA- or TC-containing wastewater. Without light or H_2O_2, negligible micropollutants (less than 5%) are decomposed. In the UVC/H_2O_2 system, the HA and TC concentrations in the effluent decrease to 0.35 and 0.20 mg L^{-1}, respectively. As the flow rate of water increases, the removal efficiency of micropollutants decreases (Fig. 5B). At 30 mL min^{-1} of flow speed, the RhB, HA and TC concentrations in the effluents are 0.15, 0.75 and 0.75 mg L^{-1}, respectively. This can be attributed to the less residence time caused by the higher flow rates. It can be expected that the removal efficiencies can be further enhanced by increasing the H_2O_2 dosages. The E_{EO} values of the pollutant decomposition in the flow-through operation are calculated according to eqn (1).[7,35] As shown in Fig. 5C, the E_{EO} values for the three pollutants are 10–60 kW h m^{-3} per order, which is comparable to the values in photo-Fenton and UV/peroxydisulfate systems (Table S2†). Considering that the electrical energy required for both H_2O_2 production and UVC/H_2O_2 processes can be replaced by sunlight and solar cells, it is promising to minimize the energy consumption in H_2O_2 production and activation. Thus, the process of coupling photocatalytic H_2O_2 production and on-site H_2O_2 activation by using UVC has great potential to be automatically operated outdoor, featuring minimum energy input, and zero maintenance and chemical addition.

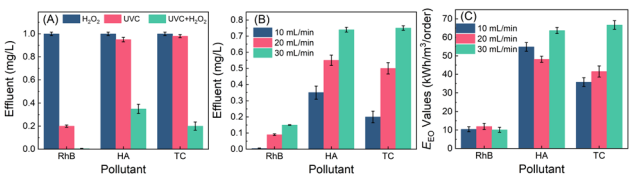

Fig. 5 (A) The concentration of micropollutants in the effluent *via* a flow-through operation (RhB, TC or HA: 1 mg L^{-1}; H_2O_2: 10 μM; flow rate: 10 mL min^{-1}; λ = 254 nm); (B) the concentration of micropollutants in the effluent *via* a flow-through operation at different flow rates; (C) E_{EO} value of RhB, HA and TC decomposition in a flow-through operation (RhB, TC or HA: 1 mg L^{-1}; H_2O_2: 10 μM; λ = 254 nm).

Conclusions

In summary, we developed a zero-chemical process to remove organic micropollutants in water *via* integrating H_2O_2 production by photocatalysis and activation by using UVC. A magnetic core–shell photocatalyst was fabricated by *in situ* growth of resorcinol–formaldehyde copolymers over silica-coated Fe_3O_4 microspheres, which can achieve 100 μmol h^{-1} H_2O_2 production from water and air over per gram MRF in the absence of organic sacrificial agents. This magnetic material can be easily separated and recycled. A UVC/H_2O_2 operation was developed by continuously mixing wastewater and the generated H_2O_2 solution, and then flowing it through a UVC reactor, which can efficiently activate H_2O_2 and degrade organic micropollutants. The process only needs light as energy input and water and air as the raw materials, representing a low-cost route to convert solar energy for environmental cleanup.

Author contributions

J. Z., Q. Z. and X. Z. designed and performed the experiments. J. Z. wrote the original draft. C. C. performed the photocatalytic performance analysis. X. G. wrote and revised the manuscript. M. L. conceived the original idea, supervised the project, and revised the manuscript.

Conflicts of interest

There are no conflicts to declare.

Acknowledgements

This work was supported by the National Natural Science Foundation of China (nos 52070128 and 22111530110).

Notes and references

1 B. C. Hodges, E. L. Cates and J. H. Kim, Challenges and prospects of advanced oxidation water treatment processes using catalytic nanomaterials, *Nat. Nanotechnol.*, 2018, **13**, 642–650.

2 H. Kim, J. Lim, S. Lee, H. H. Kim, C. Lee, J. Lee and W. Choi, Spontaneous generation of H_2O_2 and hydroxyl radical through O_2 reduction on copper phosphide under ambient aqueous condition, *Environ. Sci. Technol.*, 2019, **53**, 2918–2925.

3 X. Wang, X. Zhang, Y. Zhang, Y. Wang, S. P. Sun, W. D. Wu and Z. Wu, Nanostructured semiconductor supported iron catalysts for heterogeneous photo-Fenton oxidation: a review, *J. Mater. Chem. A*, 2020, **8**, 15513–15546.

4 K. Liu, F. A. Roddick and L. Fan, Impact of salinity and pH on the UVC/H_2O_2 treatment of reverse osmosis concentrate produced from municipal wastewater reclamation, *Water Res.*, 2012, **46**, 3229–3239.

5 H. Yao, P. Sun, D. Minakata, J. C. Crittenden and C. H. Huang, Kinetics and modeling of degradation of ionophore antibiotics by UV and UV/H_2O_2, *Environ. Sci. Technol.*, 2013, **47**, 4581–4589.

6 Y. Huang, M. Kong, S. Coffin, K. H. Cochran, D. C. Westerman, D. Schlenk, S. D. Richardson, L. Lei and D. D. Dionysiou, Degradation of contaminants of emerging concern by UV/H_2O_2 for water reuse: kinetics, mechanisms, and cytotoxicity analysis, *Water Res.*, 2020, **174**, 115587.

7 Y. Zhang, J. Zhang, Y. Xiao, V. W. C. Chang and T. T. Lim, Kinetic and mechanistic investigation of azathioprine degradation in water by UV, UV/H_2O_2 and UV/persulfate, *Chem. Eng. J.*, 2016, **302**, 526–534.

8 X. Lu, Y. Shao, N. Gao, J. Chen, H. Deng, W. Chu, N. An and F. Peng, Investigation of clofibric acid removal by UV/persulfate and UV/chlorine processes: kinetics and formation of disinfection byproducts during subsequent chlor(am)ination, *Chem. Eng. J.*, 2018, **331**, 364–371.

9 C. Baeza and D. R. Knappe, Transformation kinetics of biochemically active compounds in low-pressure UV photolysis and UV/H_2O_2 advanced oxidation processes, *Water Res.*, 2011, **45**, 4531–4543.

10 Y. Xiao, L. Zhang, W. Zhang, K. Y. Lim, R. D. Webster and T. T. Lim, Comparative evaluation of iodoacids removal by UV/persulfate and UV/H_2O_2 processes, *Water Res.*, 2016, **102**, 629–639.

11 Y. Zhang, Y. Xiao, Y. Zhong and T. T. Lim, Comparison of amoxicillin photodegradation in the UV/H_2O_2 and UV/persulfate systems: reaction kinetics, degradation pathways, and antibacterial activity, *Chem. Eng. J.*, 2019, **372**, 420–428.

12 L. H. Zheng, H. R. Su, J. Z. Zhang, L. S. Walekar, H. V. Molamahmood, B. X. Zhou, M. C. Long and Y. H. Hu, Highly selective photocatalytic production of H_2O_2 on sulfur and nitrogen for co-doped graphene quantum dots tuned TiO_2, *Appl. Catal. B*, 2018, **239**, 475–484.

13 C. Xia, Y. Xia, P. Zhu, L. Fan and H. T. Wang, Direct electrosynthesis of pure aqueous H_2O_2 solutions up to 20% by weight using a solid electrolyte, *Science*, 2019, **366**, 226–231.

14 D. B. Miklos, C. Remy, M. Jekel, K. G. Linden, J. E. Drewes and U. Hubner, Evaluation of advanced oxidation processes for water and wastewater treatment - a critical review, *Water Res.*, 2018, **139**, 118–131.

15 H. Che, X. Gao, J. Chen, J. Hou, Y. Ao and P. Wang, Iodide-induced fragmentation of polymerized hydrophilic carbon nitride for high-performance quasi-homogeneous photocatalytic H_2O_2 production, *Angew. Chem., Int. Ed.*, 2021, **60**, 25546–25550.

16 C. Chu, Q. Zhu, Z. Pan, S. Gupta, D. Huang, Y. Du, S. Weon, Y. Wu, C. Muhich, E. Stavitski, K. Domen and J. H. Kim, Spatially separating redox centers on 2D carbon nitride with cobalt single atom for photocatalytic H_2O_2 production, *Proc. Natl. Acad. Sci. U. S. A.*, 2020, **117**, 6376–6382.

17 J. Zhang, L. Zheng, F. Wang, C. Chen, H. Wu, S. A. K. Leghari and M. Long, The critical role of furfural alcohol in photocatalytic H_2O_2 production on TiO_2, *Appl. Catal. B*, 2020, **269**, 11870.

18 Y. X. Ye, J. Pan, F. Xie, L. Gong, S. Huang, Z. Ke, F. Zhu, J. Xu and G. Ouyang, Highly efficient photosynthesis of hydrogen peroxide in ambient conditions, *Proc. Natl. Acad. Sci. U. S. A.*, 2021, **118**, 2103964118.

19 Y. Zhao, P. Zhang, Z. Yang, L. Li, J. Gao, S. Chen, T. Xie, C. Diao, S. Xi, B. Xiao, C. Hu and W. Choi, Mechanistic analysis of multiple processes controlling solar-driven H_2O_2 synthesis using engineered polymeric carbon nitride, *Nat. Commun.*, 2021, **12**, 3701.

20 Y. Chen, X. Yan, J. Xu and L. Wang, K^+, Ni and carbon co-modification promoted two-electron O_2 reduction for photocatalytic H_2O_2 production by crystalline carbon nitride, *J. Mater. Chem. A*, 2021, **9**, 24056–24063.

21 W. Wang, H. Xie, G. Li, J. Li, P. K. Wong and T. An, Visible light-induced marine bacterial inactivation in seawater by an in situ photo-Fenton system without additional oxidants: implications for ballast water sterilization, *ACS ES&T Water*, 2021, **1**, 1483–1494.

22 W. Wang, W. Gu, G. Li, H. Xie, P. K. Wong and T. An, Few-layered tungsten selenide as a co-catalyst for visible-light-driven photocatalytic production of hydrogen peroxide for bacterial inactivation, *Environ. Sci.: Nano*, 2020, **7**, 3877–3887.

23 Y. Shiraishi, M. Matsumoto, S. Ichikawa, S. Tanaka and T. Hirai, Polythiophene-doped resorcinol-formaldehyde resin photocatalysts for solar-to-hydrogen peroxide energy conversion, *J. Am. Chem. Soc.*, 2021, **143**, 12590–12599.

24 Y. Shiraishi, T. Takii, T. Hagi, S. Mori, Y. Kofuji, Y. Kitagawa, S. Tanaka, S. Ichikawa and T. Hirai, Resorcinol-formaldehyde resins as metal-free semiconductor photocatalysts for solar-to-hydrogen peroxide energy conversion, *Nat. Mater.*, 2019, **18**, 985–993.

25 P. Hu, M. Long, X. Bai, C. Wang, C. Cai, J. Fu, B. Zhou and Y. Zhou, Monolithic cobalt-doped carbon aerogel for

efficient catalytic activation of peroxymonosulfate in water, *J. Hazard. Mater.*, 2017, **332**, 195–204.

26 I. Ibrar, S. Yadav, N. Ganbat, A. K. Samal, A. Altaee, J. L. Zhou and T. V. Nguyen, Feasibility of H_2O_2 cleaning for forward osmosis membrane treating landfill leachate, *J. Environ. Manage.*, 2021, **294**, 113024.

27 L. M. Rossi, N. J. S. Costa, F. P. Silva and R. Wojcieszak, Magnetic nanomaterials in catalysis: advanced catalysts for magnetic separation and beyond, *Green Chem.*, 2014, **16**, 2906–2933.

28 M. Jin, M. Long, H. Su, Y. Pan, Q. Zhang, J. Wang, B. Zhou and Y. Zhang, Magnetically separable maghemite/montmorillonite composite as an efficient heterogeneous Fenton-like catalyst for phenol degradation, *Environ. Sci. Pollut. Res.*, 2017, **24**, 1926–1937.

29 M. Usman, J. M. Byrne, A. Chaudhary, S. Orsetti, K. Hanna, C. Ruby, A. Kappler and S. B. Haderlein, Magnetite and green rust: synthesis, properties, and environmental applications of mixed-valent iron minerals, *Chem. Rev.*, 2018, **118**, 3251–3304.

30 M. Xia, C. Chen, M. Long, C. Chen, W. Cai and B. Zhou, Magnetically separable mesoporous silica nanocomposite and its application in Fenton catalysis, *Microporous Mesoporous Mater.*, 2011, **145**, 217–223.

31 M. Zhu, W. Zhang, Y. Li, L. Gai, J. Zhou and W. Ma, Multishell structured magnetic nanocomposites carrying a copolymer of pyrrole–thiophene for highly selective Au(III) recovery, *J. Mater. Chem. A*, 2016, **4**, 19060–19069.

32 S. Xuan, Y. X. Wang, J. C. Yu and K. C. Leung, Preparation, characterization, and catalytic activity of core/shell Fe_3O_4@polyaniline@au nanocomposites, *Langmuir*, 2009, **25**, 11835–11843.

33 H. Bader, V. Sturzenegger and J. Hoigné, Photometric method for the determination of low concentrations of hydrogen peroxide by the peroxidase catalyzed oxidation of N,N-diethyl-p-phenylenediamine (DPD), *Water Res.*, 1988, **22**, 1109–1115.

34 Y. Wei, J. Zhang, Q. Zheng, J. Miao, P. J. Alvarez and M. Long, Quantification of photocatalytically-generated hydrogen peroxide in the presence of organic electron donors: interference and reliability considerations, *Chemosphere*, 2021, **279**, 130556.

35 J. R. Bolton and M. I. Stefan, Fundamental photochemical approach to the concepts of fluence (UV dose) and electrical energy efficiency in photochemical degradation reactions, *Res. Chem. Intermed.*, 2002, **28**, 857–870.

36 Z. Lu, J. Dai, X. Song, G. Wang and W. Yang, Facile synthesis of Fe_3O_4/SiO_2 composite nanoparticles from primary silica particles, *Colloids Surf., A*, 2008, **317**, 450–456.

37 H. Jia, X. Zhang, X. Zeng, R. Cai, Z. Wang, Y. Yuan and T. Yue, Construction of silver nanoparticles anchored flower-like magnetic Fe_3O_4@SiO_2@MnO_2 hybrids with antibacterial and wound healing activity, *Appl. Surf. Sci.*, 2021, **567**, 150797.

38 H. Chen, C. Deng and X. Zhang, Synthesis of Fe_3O_4@SiO_2@PMMA core-shell-shell magnetic microspheres for highly efficient enrichment of peptides and proteins for MALDI-TOF MS analysis, *Angew. Chem., Int. Ed.*, 2010, **49**, 607–611.

39 N. Li, Q. Zhang, J. Liu, J. Joo, A. Lee, Y. Gan and Y. Yin, Sol-gel coating of inorganic nanostructures with resorcinol-formaldehyde resin, *Chem. Commun.*, 2013, **49**, 5135–5137.

40 Y. Deng, D. Qi, C. Deng, X. Zhang and D. Zhao, Superparamagnetic high-magnetization microspheres with an Fe_3O_4@SiO_2 core and perpendicularly aligned mesoporous SiO_2 shell for removal of microcystins, *J. Am. Chem. Soc.*, 2008, **130**, 28–29.

41 M. Shao, F. Ning, J. Zhao, M. Wei, D. G. Evans and X. Duan, Preparation of Fe_3O_4@SiO_2@layered double hydroxide core-shell microspheres for magnetic separation of proteins, *J. Am. Chem. Soc.*, 2012, **134**, 1071–1077.

42 Y. Wang, Y. Li, Z. Qiu, X. Wu, P. Zhou, T. Zhou, J. Zhao, Z. Miao, J. Zhou and S. Zhuo, Fe_3O_4@Ti_3C_2 MXene hybrids with ultrahigh volumetric capacity as an anode material for lithium-ion batteries, *J. Mater. Chem. A*, 2018, **6**, 11189–11197.

43 S. Fukuzumi, Y. M. Lee and W. Nam, Recent progress in production and usage of hydrogen peroxide, *Chin. J. Catal.*, 2021, **42**, 1241–1252.

44 F. Nemati, M. M. Heravi and R. Saeedi Rad, Nano-Fe_3O_4 encapsulated-silica particles bearing sulfonic acid groups as a magnetically separable catalyst for highly efficient Knoevenagel condensation and michael addition reactions of aromatic aldehydes with 1,3-cyclic diketones, *Chin. J. Catal.*, 2012, **33**, 1825–1831.

45 B. Zeng, L. Yang, W. Zheng, J. Zhu, X. Ma, X. Liu, C. Yuan, Y. Xu and L. Dai, Analysis of the formation process and performance of magnetic Fe_3O_4@poly(4-vinylpyridine) absorbent prepared by in-situ synthesis, *J. Mater. Sci. Technol.*, 2018, **34**, 999–1007.

46 R. Tang, T. Chen, Y. Chen, Y. Zhang and G. Wang, Core-shell TiO_2@SiO_2 catalyst for transesterification of dimethyl carbonate and phenol to diphenyl carbonate, *Chin. J. Catal.*, 2014, **35**, 457–461.

47 L. Yuan, C. Zhang, J. Wang, C. Liu and C. Yu, Mesoporous resin nanobowls with optimized donor-acceptor conjugation for highly efficient photocatalytic hydrogen peroxide production, *Nano Res.*, 2021, **14**, 3267–3273.

48 Q. Zhou, S. Ouyang, Z. Ao, J. Sun, G. Liu and X. Hu, Integrating biolayer interferometry, atomic force microscopy, and density functional theory calculation studies on the affinity between humic acid fractions and graphene oxide, *Environ. Sci. Technol.*, 2019, **53**, 3773–3781.

49 J. Zhang, J. Lang, Y. Wei, Q. Zheng, L. Liu, Y. H. Hu, B. Zhou, C. Yuan and M. Long, Efficient photocatalytic H_2O_2 production from oxygen and pure water over graphitic carbon nitride decorated by oxidative red phosphorus, *Appl. Catal. B*, 2021, 120522.

50 W. Liu, P. Wang, J. Chen, X. Gao, H. Che, B. Liu and Y. Ao, Unraveling the mechanism on ultrahigh efficiency photocatalytic H_2O_2 generation for dual-heteroatom incorporated polymeric carbon nitride, *Adv. Funct. Mater.*, 2022, **32**, 2205119.

51 Y. Wu, J. Chen, H. Che, X. Gao, Y. Ao and P. Wang, Boosting $2e^-$ oxygen reduction reaction in garland carbon nitride with carbon defects for high-efficient photocatalysis-self-Fenton degradation of 2,4-dichlorophenol, *Appl. Catal., B*, 2022, **307**, 121185.

52 J. Brame, M. Long, Q. Li and P. Alvarez, Trading oxidation power for efficiency: differential inhibition of photo-generated hydroxyl radicals versus singlet oxygen, *Water Res.*, 2014, **60**, 259–266.

53 A. Di Cesare, M. De Carluccio, E. M. Eckert, D. Fontaneto, A. Fiorentino, G. Corno, P. Prete, R. Cucciniello, A. Proto and L. Rizzo, Combination of flow cytometry and molecular analysis to monitor the effect of UVC/H_2O_2 vs. UVC/H_2O_2/Cu-IDS processes on pathogens and antibiotic resistant genes in secondary wastewater effluents, *Water Res.*, 2020, **184**, 116194.